PHYSICAL REVIEW D **103,** 083005 (2021)

Modeling and searching for a stochastic gravitational-wave background from ultralight vector bosons

Leo Tsukada,[1,2,*] Richard Brito,[3] William E. East,[4] and Nils Siemonsen[4,5]

[1]*Research Center for the Early Universe (RESCEU), Graduate School of Science, The University of Tokyo, Tokyo 113-0033, Japan*
[2]*Department of Physics, Graduate School of Science, The University of Tokyo, Tokyo 113-0033, Japan*
[3]*Dipartimento di Fisica, "Sapienza", Università di Roma and Sezione INFN Roma1, Piazzale Aldo Moro 5, 00185 Roma, Italy*
[4]*Perimeter Institute for Theoretical Physics, Waterloo, Ontario N2L 2Y5, Canada*
[5]*Department of Physics and Astronomy, University of Waterloo, Waterloo, Ontario N2L 3G1, Canada*

(Received 15 November 2020; accepted 1 March 2021; published 6 April 2021)

Ultralight bosons, which are predicted in a variety of beyond-Standard-Model scenarios as dark-matter candidates, can trigger superradiant instability around spinning black holes. This instability gives rise to oscillating boson condensates, which then dissipate through the emission of nearly monochromatic gravitational waves. Such systems are promising sources for current and future gravitational-wave detectors. In this work, we consider minimally coupled, massive vector bosons, which can produce a significantly stronger gravitational-wave signal compared to the scalar case. We adopt recently obtained numerical results for the gravitational-wave flux, and astrophysical models of black-hole populations that include both isolated black holes and binary merger remnants, to compute and study in detail the stochastic gravitational-wave background emitted by these sources. Using a Bayesian framework, we search for such a background signal emitted using data from the first and second observing runs of Advanced LIGO. We find no evidence for such a signal. Therefore, the results allow us to constrain minimally coupled vector fields with masses in the range 0.8×10^{-13} eV $\leq m_b \leq 6.0\times10^{-13}$ eV at 95% credibility, assuming optimistically that the dimensionless spin distribution for the isolated black-hole population is uniform in the range [0, 1]. With more pessimistic assumptions, a narrower range around $m_b \approx 10^{-13}$ eV can still be excluded as long as the upper end of the uniform distribution for dimensionless black-hole spin is $\gtrsim 0.2$.

DOI: 10.1103/PhysRevD.103.083005

I. INTRODUCTION

The detection of gravitational waves (GWs) emitted by binary black-hole (BBH) and binary neutron star coalescence events [1–13] has opened a new era of discoveries with far-reaching implications for astrophysics [14–17] and fundamental physics [16,18–23]. In the very near future [24], Advanced LIGO [25] and Advanced Virgo [26] will be joined in observing by additional detectors, such as KAGRA [27] and LIGO-India [28], and there are plans for a third generation of ground-based detectors [29,30]. Together with the planned space-based GW detectors LISA [31] and pulsar-timing arrays [32], this will allow us to access a large range of the GW frequency spectrum.

A major target for this network of detectors is the detection of a stochastic gravitational-wave background (SGWB) produced by the incoherent superposition of many sources too faint to be resolved individually (see, e.g., [33] for a recent review). In the LIGO/Virgo frequency band, one of the most promising targets is the background emitted by compact binary coalescences (CBCs) [34–37]. Here, we consider another possible source for the SGWB that would be present if ultralight bosons in certain mass ranges exist in the Universe [38,39] (see also Ref. [40]).

The main mechanism responsible for this SGWB is the superradiant instability of spinning black holes (BHs) in the presence of massive bosons [41–60]. The superradiant instability relies on the fact that massive bosons with rest mass m_b can form (quasi)bound states around BHs with oscillation frequency $\omega_R \sim m_b c^2/\hbar$, allowing for continuous energy extraction whenever ω_R satisfies the *superradiant condition*

$$0 < \omega_R < m\Omega_H, \tag{1}$$

where m is the azimuthal index of the boson field and Ω_H is the BH's horizon angular velocity (see Ref. [61] for a review). As the system becomes unstable, the boson modes start growing exponentially. The superradiant instability is most effective when the boson's reduced Compton

---

[*] tsukada@resceu.s.u-tokyo.ac.jp

wavelength $\lambdabar \equiv \hbar/(m_b c)$ is comparable to the BH's gravitational radius $r_g \equiv 2GM/c^2$, i.e., when

$$m_b c^2 \sim \frac{\hbar c^3}{2GM} \sim 10^{-12}\ \mathrm{eV} \times \left(\frac{M}{70\ \mathrm{M}_\odot}\right)^{-1}, \qquad (2)$$

for a BH with mass M. In general, for a given boson rest mass, only for a relatively narrow window of BH masses will the superradiant instability timescale be sufficiently short in an astrophysical context (see, e.g., Ref. [61]).

During the instability phase, the BH spins down, transferring energy and angular momentum to the boson field until the point where the superradiant condition saturates $\omega_R \sim \Omega_H$, resulting in the formation of an oscillating nonaxisymmetric boson "cloud" which acts as a source of nearly monochromatic GWs with frequency

$$f_{\mathrm{GW}} \sim \omega_R/\pi \sim 484\ \mathrm{Hz}\left(\frac{m_b c^2}{10^{-12}\ \mathrm{eV}}\right). \qquad (3)$$

Combining the above equation with Eq. (2), it follows that Advanced LIGO is especially sensitive to the GW emission from bosons with $m_b \sim \mathcal{O}(10^{-12})$ eV surrounding BHs with masses from $\mathcal{O}(10)$ $\mathrm{M}_\odot$ up to $\mathcal{O}(100)$ $\mathrm{M}_\odot$. These GWs have been shown to be observable with current and future ground-based GW detectors in two regimes—a "resolvable" regime, in which nearby sources can be directly detected [45,54,60,62–71], and an "unresolvable" regime, where the incoherent superposition of all other sources in the Universe contribute to a SGWB [38,39,60,65].

These considerations are especially important given that light boson fields in a wide range of masses have been proposed as potential dark-matter candidates [45,72–76] and are predicted in many extensions to the Standard Model of particle physics [45,72,75,77–80]. Prototypical examples include not only the hypothetical QCD axion [81,82] and axionlike particles arising in string theory scenarios [45], but also models involving ultralight vector fields, such as dark photons as dark-matter candidates [72,79,80, 83–85], and more generic hidden vector fields which also arise as a generic prediction of string theory [77]. Being a purely gravitational effect, the superradiant instability and subsequent GW emission from boson clouds provide a powerful way to search for such particles and complement more conventional searches which normally rely on (nongravitational) couplings of these fields with Standard Model particles.

Most studies and searches for GW signals from boson clouds in LIGO data have so far focused on massive scalar fields. In particular, Ref. [39] conducted a search for the SGWB model in the data from LIGO's first observation run. No signal was found, which allowed them to constrain scalar fields with masses in the range 2.0×10^{-13} to 3.8×10^{-13} eV in an optimistic scenario. Excluding some range of ultralight boson masses in the absence of the detection of GW signal requires one to make assumptions about the BH population and, in particular, the BH spin distribution. Similarly in this work, we will consider several different ways of parameterizing the unknown BH population statistics. Searches for (resolvable) continuous GWs emitted by individual BH-scalar cloud systems have also been conducted [67,70,71], but no signal has been found so far either, suggesting constraints on scalar bosons in a similar mass range ($\sim[10^{-13}, 10^{-12}]$ eV).

Making use of recent theoretical developments in the understanding of superradiant instabilities from vector fields [57,58,86], in this paper, we extend those results by modeling in detail the SGWB emitted by vector fields and searching for this signal in Advanced LIGO's data. Compared to the scalar field case, the superradiant instability and GW emission timescales for vector fields can be significantly shorter. Intuitively, this is because ultralight vector clouds can carry spin angular momentum (while scalar clouds can carry only orbital angular momentum), and, thus, vectors form more compact clouds with greater fluxes across the BH horizons. As we will show, these faster timescales allow us to constrain a wider range of boson masses.

This paper is structured as follows. In Sec. II, we provide a brief overview of the superradiant instability and subsequent GW emission by massive vector bosons presented in Ref. [86]. In Sec. III, we discuss in detail the predicted SGWB signal from vector clouds and compare it to the scalar field case. In Sec. IV, we present the Bayesian framework that we use to search for this background in GW data. Using this framework, in Sec. V, we study the vector mass range that this search method is sensitive to and explore the capacity of Bayesian model selection to distinguish between the background due to the superradiant instability and that due to unresolved CBCs. A search using real data is presented in Sec. VI, where we show the range of excluded vector masses using data from Advanced LIGO's first and second observing runs. Finally, Sec. VII summarizes our findings and the implications of our results.

In what follows, we use units $G = c = 1$ unless otherwise stated.

II. SUPERRADIANT INSTABILITY AND GW EMISSION

In this section, we briefly review how a vector cloud would spontaneously grow around a spinning BH through the superradiant instability, eventually saturate, and then dissipate through the emission of GWs. The superradiant instability can occur for bosons with spin 0 (scalar) [38,41–44,63–65,87] or spin 1 (vector) [48,52–56,59] (see also Refs. [50,60] for massive spin-2 fields). The qualitative picture is the same in either case, the main difference being the generically shorter timescales for the vector field case.

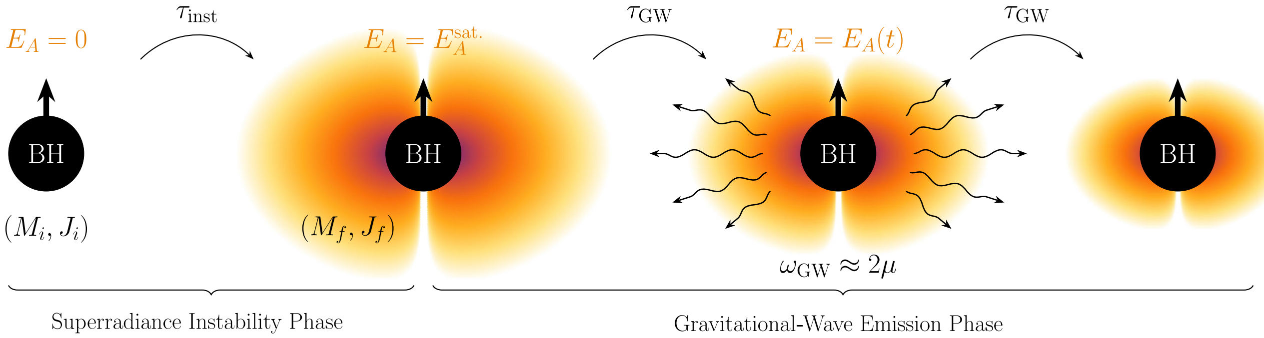

FIG. 1. A schematic representation of the evolution of the superradiance instability and subsequent GW emission. Initial (e.g., quantum) fluctuations in the Proca field seed the instability, leading to an exponentially growing boson cloud around the spinning BH (with growth timescale $\tau_{\rm inst}$). The Proca cloud grows at the expense of BH angular momentum and mass: $M_i - M_f = E_A^{\rm sat} > 0$. After saturation, in the GW emission phase the cloud slowly decays with timescale $\tau_{\rm GW}$ by emitting monochromatic gravitational radiation at frequency $\omega_{\rm GW} \approx 2\mu$ [see also Eq. (12)], until the cloud's mass is too small to emit detectable GWs or an unstable higher azimuthal mode begins dominating the dynamics.

We then describe our specific model for the GW signal from a vector cloud, which is based on Ref. [86].

A. Evolution of the Proca cloud

We consider a single (*real*) massive vector A_μ, or Proca field, which is minimally coupled, and ignore any coupling with Standard Model particles, as well as any nontrivial self-interactions beyond the mass term. Around a spinning BH, bound Proca states with oscillation frequency ω_R satisfying Eq. (1) can spontaneously grow, exhibiting exponential growth with imaginary frequency ω_I. The BH-cloud system is then characterized by three distinct timescales: the oscillation timescale $\tau_{\rm osc} = \omega_R^{-1}$, the superradiant instability growth timescale $\tau_{\rm inst} = \omega_I^{-1}$, and the GW emission timescale $\tau_{\rm GW}$ (defined below). The hierarchy of these timescales, $\tau_{\rm osc} \ll \tau_{\rm inst} \ll \tau_{\rm GW}$, enables us to treat the extraction of angular momentum from the spinning BH in a quasiadiabatic form and ignore gravitational radiation during the evolution of the superradiant instability [88]. See Fig. 1 for a cartoon representation of the dynamics of the BH-cloud system from the onset of the superradiant instability, through saturation and to the GW emission phase. Assuming that the instability is triggered by some small initial Proca field configuration [e.g., a quantum fluctuation with $\mathcal{O}(1)$ massive vector bosons], it grows exponentially with timescale $\tau_{\rm inst}$. In the limit $M\mu \ll 1$, the typical instability timescales are roughly given by (see, e.g., [59])

$$\tau_{\rm inst}^S \approx 30\ {\rm days} \left(\frac{M}{10\ {\rm M}_\odot}\right)\left(\frac{0.1}{M\mu}\right)^9\left(\frac{0.9}{\chi_i}\right), \tag{4}$$

$$\tau_{\rm inst}^V \approx 280\ {\rm s} \left(\frac{M}{10\ {\rm M}_\odot}\right)\left(\frac{0.1}{M\mu}\right)^7\left(\frac{0.9}{\chi_i}\right), \tag{5}$$

where the superscripts S and V each stand for the scalar and vector field case, respectively. While doing so, it extracts angular momentum δJ from the Kerr BH. For linear fluxes across the BH horizon, it follows that $\delta J = m\tau_{\rm osc}\delta M$. Hence, we can assume that the BH-cloud system moves through a sequence of Kerr spacetimes with decreasing angular momentum J and mass M (but *increasing* irreducible mass).

The amplitude of the Proca field A_μ increases by roughly 180 e-folds from the onset of the instability to saturation. As was noted in Refs. [53,56,89], the BH-cloud system is well modeled by the *linear* Proca solution on the background of a Kerr BH with mass and angular momentum that slowly decreases until the synchronization criterion

$$\Omega_H(M_f, J_f) = \Omega_H(M_i + \delta M, J_i + \delta J) = \omega_R/m \tag{6}$$

is satisfied and the instability shuts off. Here, M_i and J_i are the initial BH mass and angular momentum, respectively, M_f and J_f are the final BH parameters, and $\Omega_H(M,J) = J/[2M(M^2 + (M^4 - J^2)^{1/2})]$ is the BH horizon frequency. This expression, combined with knowledge of ω_R (which has implicit dependence on M and J), determines the energy $E_A^{\rm sat} = -\delta M$ that is extracted from the BH. Depending on the parameters, the cloud can contain up to ∼10% of the original BH's mass, while oscillating with frequency ω_R around the BH. This induces strong gravitational radiation that can potentially be observed.[1] After saturation, the only dynamical timescales are $\tau_{\rm osc}$ and $\tau_{\rm GW}$. Since the GW power is proportional to the square of the cloud energy, $\dot{E}_{\rm GW} \propto E_A^2$, the cloud energy reduces as

---

[1] Note that a *complex* massive vector field undergoes the same exponential growth as its real counterpart. However, if the real and imaginary components of the field are arranged such that the resulting stress-energy distribution is axisymmetric (assuming similar initial conditions as above), the GW emission is highly suppressed compared to the case considered here [53].

$$E_A(t) = \frac{E_A^{\rm sat}}{1 + t/\tau_{\rm GW}}, \quad \tau_{\rm GW} = \frac{E_A^{\rm sat}}{\dot{E}_{\rm GW}(t = t_{\rm sat})}. \tag{7}$$

The GW power for vector clouds is to be contrasted with the scalar field case, for which the GW power is much smaller [86]. This difference in the GW power translates in a large difference in the typical GW emission timescale, of which the nonrelativistic estimates (i.e., $M\mu \ll 1$) roughly read

$$\tau_{\rm GW}^S \approx 10^5 \ {\rm yr}\left(\frac{M}{10 \ {\rm M}_\odot}\right)\left(\frac{0.1}{M\mu}\right)^{15}\left(\frac{0.5}{\chi_i - \chi_f}\right), \tag{8}$$

$$\tau_{\rm GW}^V \approx 8 \ {\rm days}\left(\frac{M}{10 \ {\rm M}_\odot}\right)\left(\frac{0.1}{M\mu}\right)^{11}\left(\frac{0.5}{\chi_i - \chi_f}\right), \tag{9}$$

where again the superscripts S and V each stand for the scalar and vector field case, respectively, and χ_i and χ_f stand for the BH spin at the birth and the end of the instability phase, respectively. Comparing these to the instability timescales [Eqs. (4) and (5)], it clearly follows that $\tau_{\rm GW} \gg \tau_{\rm inst}$, and, hence, during the exponential evolution of the Proca cloud, the GW emission can be neglected. This is true even beyond the nonrelativistic regime [86].

B. Proca-BH bound states

In our approach, which follows closely the Proca mode analysis in Refs. [58,86], we use BH perturbation theory to compute the bound Proca states. The underlying field equations are

$$\nabla_\alpha F^{\alpha\beta} = \mu^2 A^\beta, \tag{10}$$

where $F_{\alpha\beta} = 2\nabla_{[\alpha}A_{\beta]}$ is the Proca field strength tensor, $\mu = m_b/\hbar$, and geometric quantities are computed using the Kerr metric of a spinning BH. Lunin discovered a separation ansatz in Ref. [90] for the Maxwell equations in Kerr spacetimes (and generalizations thereof) that makes a direct reconstruction of the 4-potential trivial after solving the respective second-order ordinary differential equations (ODEs).[2] In Refs. [57,92], this ansatz was shown to separate the massive vector field equations in Kerr spacetimes (which are not separable in the Teukolsky formalism). The vector potential ansatz takes the form

$$A^\mu = B^{\mu\nu}\nabla_\nu Z, \qquad Z = e^{-i\omega t + im\varphi}R(r)S(\theta), \tag{11}$$

where $B^{\mu\nu}$ is a polarization tensor constructed from the hidden symmetries of the Kerr-NUT-(A)dS family of spacetimes (see Ref. [58] for the explicit form used here). With this ansatz, Eq. (10) reduces to two separated ODEs parameterized by the vector boson mass $M\mu$ and dimensionless BH spin $\chi = J/M^2$ and coupled only by the respective separation constants: the azimuthal mode number $m \geq 1$, the overtone number $\hat{n} \geq 0$, the polarization state $S \in \{-1, 0, 1\}$, and the real and imaginary parts of the frequency $\omega = \omega_R + i\omega_I$.

In the nonrelativistic limit, i.e., if $M\mu \ll 1$ [47,48,54,55,59],

$$\omega_R = \mu\left(1 - \frac{\mu^2 M^2}{2(|m| + \hat{n} + S + 1)^2}\right) + \mathcal{O}[(M\mu)^4], \tag{12}$$

$$\omega_I = C_{m,\hat{n},S}(J, M, \omega_R)(M\mu)^{4m+2S+5}(\omega_R - m\Omega_H), \tag{13}$$

where $C_{m,\hat{n},S}(J, M, \omega_R)$ is a set of coefficients [54,55,59] and the modes with $S = -1$ polarization, $\hat{n} = 0$, and lowest value of m that satisfies $\omega_R < m\Omega_H$ are the most unstable (fastest growing). Here, we focus on such modes and restrict to $m = 1$ and 2.[3] Note that, in the nonrelativistic limit, the fastest growing vector mode corresponds to a hydrogenlike cloud with orbital number $\ell = 0$ spatial dependence, but with $j = m = 1$, due to the spin contribution, where j is the total angular momentum number [54]. In contrast, the fastest growing scalar mode has $\ell = 1$, and, therefore, the cloud sits farther from the BH due to the centrifugal barrier. Hence, in the vector case, the relative flux across the BH horizon is greater, leading to faster superradiant growth, and the cloud is more compact, leading to greater gravitational radiation.

We additionally restrict ourselves to GWs emitted by BH-cloud systems in the saturated state (again due to the hierarchy of timescales mentioned above). This implies that the angular momentum dependency of ω can be removed by solving for $J_{\rm sat.}$ using Eq. (6). We thus need only the real frequency ω_R and can ignore the instability timescale. (For a detailed analysis of the growth rates as a function of Proca mass and BH spin in the relativistic regime, see Refs. [52,55,57,58,86].) We use the numerical data in Ref. [86], obtained from solving the Proca field equations as described above for the marginally unstable modes, to fit the following functional form, which already includes the leading-order, nonrelativistic behavior:

$$\frac{\omega_R^{\rm sat}}{\mu} = 1 - \frac{(M\mu)^2}{2m^2} + \sum_{\alpha=4}^{10} c_\alpha^m (M\mu)^\alpha, \tag{14}$$

---

[2] This can be contrasted with the well-established Teukolsky formalism [91] that provides only a single polarization and requires an elaborate reconstruction mechanism to construct the 4-potential.

[3] We note that, as shown in Ref. [86], there are regions of the parameter space where the fundamental mode ($\hat{n} = 0$) grows slower than one or more of the overtones for $m \geq 2$ in the relativistic regime. This raises the possibility of several modes being populated simultaneously, generating a unique beating GW signal. We do not consider such signals here, since they will have a small contribution to the stochastic GW background.

TABLE I. The coefficients c^m_α, defined in Eq. (14), of the higher-order terms in ω_R for the $m = 1$ and $m = 2$ mode, respectively.

$m\backslash\alpha$	4	5	6	7	8	9	10
1	−2.56	13.85	−97.65	349.53	−615.29	532.55	−183.08
2	−0.076	0.0071	0.029	−0.051	0.14	−0.12	0.034

where the fitted coefficients are given in Table I (see also Appendix A in Ref. [86] for fits covering the whole parameter space). This value is used to compute the saturation energy and angular momentum of the cloud, as well as the GW frequency, as described below.

C. Gravitational radiation

In order to compute the GW power from the boson cloud, we use the stress-energy tensor calculated from the Proca field solutions described above and numerically solve the Teukolsky equation for the GW perturbations with this as a source. See Ref. [86] for details. Since the stress-energy is quadratic in the field, the (angular) frequency of the GW radiation is $\omega_{\rm GW} = 2\omega_R$. The angular dependence of the GWs has spheroidal harmonic components with azimuthal number $\pm 2m$ and is dominated by the $\ell = 2m$ contribution, though higher ℓ components can be significant in the relativistic and high-spin regime (and are included in our calculation of the power). Because the GW energy flux scales as $\dot{E}_{\rm GW} \propto E_A(t)^2$ in this treatment, we can phrase these results in terms of the mass-rescaled (dimensionless) GW power $\dot{\tilde{E}}_{\rm GW} = \dot{E}_{\rm GW} \times (M/E_A)^2$. In the relativistic regime—in particular, for $M\mu > 0.05$ if $m = 1$ and $\mu M > 0.67$ if $m = 2$—we use the following polynomial fitting function for convenience:

$$\dot{\tilde{E}}^m_{\rm GW} = \sum_{\alpha=0}^{N_m} d^m_\alpha (M\mu)^\alpha, \tag{15}$$

where the respective coefficients, determined from the numerical data of Ref. [86], are given in Table II. In order to extrapolate our results to the nonrelativistic limit, we use the following expressions:

$$\dot{\tilde{E}}^{m=1}_{\rm GW} = 1.3 \times 10^{-12} \left(\frac{M\mu}{0.05}\right)^{10}, \qquad M\mu \leq 0.05,$$
$$\dot{\tilde{E}}^{m=2}_{\rm GW} = \frac{(M\mu)^{14}}{1.0 \times 10^5} + 6.4 \times 10^{-4} (M\mu)^{16}, \qquad M\mu \leq 0.67. \tag{16}$$

The exponent of the lowest-order term in the respective expressions was chosen to match that of the analytic calculation in Ref. [54], but the coefficients were determined by fitting against the numerical data of Ref. [86] up to $M\mu \approx 0.1$ (0.7) for $m = 1$ (2), respectively (since even in nonrelativistic limit one expects leading-order corrections to the flat space results in Ref. [54]). Because the GW power is heavily suppressed in this regime, our results are not overly sensitive to how this extrapolation is done.

TABLE II. The coefficients d^m_α for the GW power ansatz in Eq. (15), fitted against the numerical data of Ref. [86]. Here, $N_{m=1} = 10$ and $N_{m=2} = 14$.

$m\backslash\alpha$	0	1	2	3	4	5	6	7	8	9	10	11	12	13	14
1	-9.6×10^{-6}	−0.000064	0.018	−0.27	2.36	−12.8	41.5	−76.9	70.0	−15.9	−10.2	⋯	⋯	⋯	⋯
2	−0.00014	−0.019	0.080	0.00011	1.00	−1.95	−9.31	60.5	−165.1	275.5	−304.2	−224.6	−107.1	29.9	−3.72

Finally, the total GW energy emitted over a time Δt is given by

$$E_{\rm GW} = \int_{t=0}^{\Delta t} {\rm d}t \frac{{\rm d}E_{\rm GW}}{{\rm d}t} = \frac{E_A^{\rm sat} \Delta t}{\Delta t + \tau_{\rm GW}}. \tag{17}$$

For our purposes, we will define the signal duration to be the lifetime of each BH, namely, $\Delta t = t_0 - t(z_f)$, where t_0 is the age of the Universe, $t_0 \approx 13.8$ Gyr, and $t(z_f)$ is the cosmic time at the redshift of the BH formation. For all cases of interest, the instability timescale is much smaller than the BH lifetime, so we neglect the small delay between BH formation and saturation of the superradiant instability. For BHs whose age is comparable to the instability timescale, the overestimated GW radiation is negligibly small in any case, and, therefore, this approximation does not affect our estimate of the overall energy density $\Omega_{\rm GW}$. The SGWB is then determined from summing over the energy emitted by each BH-cloud system over the population of spinning BHs, as we describe in the next section.

III. MODELING THE STOCHASTIC BACKGROUND

In this section, we describe our SGWB model from the whole population of BH-cloud systems. The model follows the construction in Refs. [38,39], where the superradiant instability of ultralight scalar bosons was considered. In particular, we will see that some differences between the background emitted by scalar and vector clouds arise, mainly due to the larger GW power emitted by vector bosons when compared to the scalar case.

A. General formulation

Under the assumptions that the SGWB is (a) isotropic, (b) unpolarized, (c) stationary, and (d) Gaussian, the background spectrum can be described in terms of the GW energy density per logarithmic frequency interval. This can be computed by integrating the SGWB spectrum from individual sources over the entire population [93]:

$$\Omega_{\rm GW}(f) \equiv \frac{1}{\rho_c}\frac{{\rm d}\rho_{\rm GW}}{{\rm d}\ln(f)} = \frac{f}{\rho_c}\int {\rm d}z\frac{{\rm d}t}{{\rm d}z}\int {\rm d}\boldsymbol{\theta}\, p(\boldsymbol{\theta})R(z;\boldsymbol{\theta})\frac{{\rm d}E_s}{{\rm d}f_s}(\boldsymbol{\theta}). \tag{18}$$

Here, ρ_c is the critical energy density required to have a spatially flat universe, $R(z;\boldsymbol{\theta})$ is the event rate of GW emission per unit comoving volume per unit *source frame* time, and $p(\boldsymbol{\theta})$ is the multivariate probability distribution of the source parameters $\boldsymbol{\theta}$. Since the individual sources emit GWs with nearly constant frequencies, the energy spectrum from individual signals can be approximated by

$$\frac{{\rm d}E_{\rm s}}{{\rm d}f_s} \approx E_{\rm GW}\delta(f(1+z) - f_0), \tag{19}$$

where $f_0 = \omega_R/\pi$ [computed using Eq. (14)] and $E_{\rm GW}$ is given by Eq. (17). Note that, due to the cosmological redshift z, the observed frequency f is related to the source frame frequency f_s such that $f = f_s/(1+z)$.

B. BH population models

To compute the stochastic background, we consider two possible BH formation channels: isolated extragalactic BHs and BBH merger remnants. We treat their contribution to the total GW energy density independently. Importantly, we do not consider the galactic BH population (e.g., as recently described in Ref. [71]), as our method to search for a SGWB (described in Sec. IV) is optimized for a Gaussian distributed signal. The signal emitted from galactic BHs is expected to add a mostly non-Gaussian and nonisotropically distributed component to the stochastic background.[4] This non-Gaussian component would typically be vetoed in the process of data conditioning in the SGWB search pipeline we use [94]. Studying the specific features of this component goes beyond the scope of this paper, but adding it to the search pipeline is certainly an important addition for future work and could make the constraints we here present even stronger.

Let us then briefly explain the prescription for each channel (see Ref. [39] for more details). In the isolated BH channel, Eq. (18) can be written as

$$\Omega^{\rm iso}_{\rm GW}(f) = \frac{f}{\rho_c}\int {\rm d}z\frac{{\rm d}t}{{\rm d}z}\int {\rm d}M{\rm d}\chi\, p(\chi)\frac{{\rm d}\dot{n}}{{\rm d}M}\frac{{\rm d}E_s}{{\rm d}f_s}, \tag{20}$$

where $\frac{{\rm d}\dot{n}}{{\rm d}M}$ is the BH formation rate per BH mass, which we construct following Ref. [39] using a BH mass function that spans masses in the range [3–60] $M_\odot$. Since not much is known about the spin distribution at birth of isolated BHs,[5] for the probability density of the natal BH spin χ we assume a uniform distribution

$$p(\chi) = \begin{cases} 0 & (\chi < \chi_{\rm ll}, \chi_{\rm ul} < \chi), \\ \frac{1}{\chi_{\rm ul}-\chi_{\rm ll}} & (\chi_{\rm ll} \le \chi \le \chi_{\rm ul}), \end{cases} \tag{21}$$

where $\chi_{\rm ll}$ and $\chi_{\rm ul}$ are the lower and upper limit of the distribution, respectively. Given that these limits in the natal spin distribution of isolated BHs are extremely uncertain, for simplicity when searching for this SGWB, we will parametrize the distribution in two different ways: (a) leave the lower limit $\chi_{\rm ll}$ as a free parameter but fix $\chi_{\rm ul} = 1$; (b) leave the upper limit $\chi_{\rm ul}$ as a free parameter but fix $\chi_{\rm ll} = 0$. In the remainder of the text, we will denote these parametrizations as the $\chi_{\rm ll}$ and $\chi_{\rm ul}$ parametrizations, respectively. In general, the first case allows for a larger amplitude for the background than the second case, since it ensures a population of BHs born with high spin, from which it is possible to extract more energy through the superradiant instability. Different choices for $\chi_{\rm ll,ul}$ can significantly affect the background spectrum. Hence, as we will show in Sec. VI, constraints on the vector boson mass obtained when searching for such background in LIGO data crucially depend on the parametrization one uses.

For the BBH merger remnant channel, Eq. (18) reduces to

$$\Omega^{\rm rem}_{\rm GW}(f) = \frac{f}{\rho_c}\int {\rm d}z\frac{{\rm d}t}{{\rm d}z}\times\int {\rm d}\boldsymbol{m}{\rm d}\chi\, p(\boldsymbol{m})R_m(z;\boldsymbol{m})p(\chi)\frac{{\rm d}E_s}{{\rm d}f_s}, \tag{22}$$

where $\boldsymbol{m}$ denotes the component masses of the BBH system, $p(\boldsymbol{m})$ is the component mass distribution, and $R_m(z;\boldsymbol{m})$ is the BBH merger rate density for a given $\boldsymbol{m}$ and cosmological redshift z. Compared to the spin distribution of isolated BHs, the spin distribution $p(\chi)$ for this channel can be more easily constrained, using measurements of the spin of remnant BHs observed by Advanced LIGO and Virgo [1–6,8,9,12]. For a population of merging BHs dominated by near-equal mass BHs that are not rapidly spinning, as the majority of the observations made so far suggest, the spin magnitude of the final remnant BHs is

---

[4] We should also note that, for a given boson mass, the GW signals emitted by the galactic population would tend to accumulate in a very narrow frequency window around ω_R [see Eq. (3)] [71], unlike the extragalactic component which should be spread over a broader range of frequencies due to the cosmological redshift. Our search method is better suited for signals that emit in a broad range of frequencies.

[5] Some predictions for the natal BH spin distribution can be found in Ref. [95] (see their Figs. 1 and 2), where it is shown that the BH spin distribution depends very strongly on the assumed model for the angular momentum transport in the progenitor stars.

clustered around 0.7 [96,97]. Therefore, for simplicity, we assume that all the remnant BHs initially have $\chi = 0.7$, that is,

$$p(\chi) = \delta(\chi - 0.7). \tag{23}$$

To model the BBH merger rate, we follow the prescription described in Refs. [34,37], calibrating it with the local merger rate inferred from the BBHs detected in the first two observing runs[6] of Advanced LIGO and Virgo. We adopt the rate estimated in Ref. [8], in particular, the one derived from the BH mass function with a power law distribution, such that

$$\int p(\boldsymbol{m}) R_m(z = 0; \boldsymbol{m}) \mathrm{d}\boldsymbol{m} = 56\ \mathrm{Gpc}^{-3}\ \mathrm{yr}^{-1}. \tag{24}$$

The two assumptions made above contribute to a systematic uncertainty in the prediction of the energy density spectrum, $\Omega_{\mathrm{gw}}^{\mathrm{rem}}(f)$. However, as we will show in the next subsection, the contribution from the BBH remnant channel is subdominant (compared to the isolated BH channel) for the range of vector masses to which current GW detectors are sensitive. Therefore, this uncertainty does not affect the results from our search and, hence, the constraints on the vector boson mass.

C. Total background model

We derive the total background by summing over the contributions from the two channels, namely,

$$\Omega_{\mathrm{GW}}(f) = \Omega_{\mathrm{GW}}^{\mathrm{iso}}(f) + \Omega_{\mathrm{GW}}^{\mathrm{rem}}(f), \tag{25}$$

where the superscripts represent each of the isolated BH and BBH merger remnant populations defined by Eqs. (20) and (22), respectively. Figure 2 compares the contribution to the total energy density spectrum from each of these two channels, where we assumed a uniform distribution for the natal BH spin $\chi \in [0, 1]$ in the isolated BH channel. As one can see, the isolated BH channel (solid lines) dominates over the BBH merger remnant channel (dashed lines) for $m_b \gtrsim 10^{-13.5}$ eV, corresponding to frequencies $\gtrsim$10 Hz. Since current GW detectors are mainly sensitive in this frequency range (see Fig. 4), the detectable SGWB from ultralight vector bosons is expected to be dominated by the isolated BH channel.

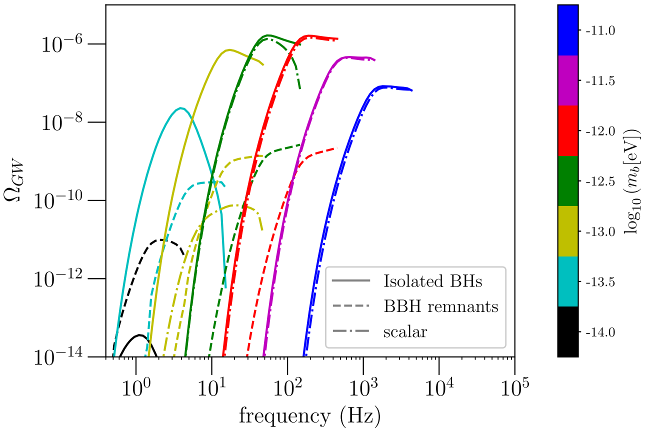

FIG. 2. Contribution of different BH formation channels for the total background spectrum Ω_{GW}. Solid curves correspond to the spectrum from the isolated BH channel with different boson masses represented by the color bar assuming a uniform distribution for the initial BH spin $\chi \in [0, 1]$, whereas dashed curves show the spectrum due to the BBH merger remnant channel. For comparison, we also show the total energy spectra that scalar bosons with mass $m_b \geq 10^{-13.5}$ eV would give rise to (dash-dotted lines), including both BH formation channels, and assuming the same BH mass and spin distribution as in the vector case.

For completeness, in Fig. 2 we also compare the backgrounds emitted by vector bosons against those produced by scalar bosons (dash-dotted lines) considered in Refs. [38,39]. For $m_b > 10^{-12.5}$ eV, both cases predict almost identical spectra. This is because, in both cases, the typical instability and GW emission timescales for these boson masses are sufficiently short, such that, for most BHs that become superradiantly unstable, almost all the energy in the cloud is dissipated away in GWs within the lifetime of the BHs we consider in our population models. Since the total amount of energy that can be extracted through the superradiant instability is nearly independent of the boson spin, it therefore follows that total energy emitted in GWs by the whole BH population should be almost independent of the boson spin for boson masses $m_b > 10^{-12.5}$ eV.

On the other hand, for $m_b \lesssim 10^{-12.5}$ eV, there can be significant differences between the background predicted in the scalar field case and the one due to a vector field. For $m_b = 10^{-12.5}$ eV, this difference is more pronounced at larger frequencies because of the fact that the GWs emitted at higher frequencies are typically sourced by BHs at smaller redshifts [see Eq. (19)] and, hence, BHs with smaller lifetimes. Since the typical GW emission timescale for scalar bosons is larger than that for vector bosons, the total energy emitted in GWs for those BHs tends to be smaller for the scalar case than the vector case, hence the difference at higher frequencies seen for $m_b \lesssim 10^{-12.5}$ eV. For lighter boson masses ($m_b < 10^{-12.5}$ eV), the amplitude of the background predicted in the scalar field case tends to be much smaller than for vector fields, because for those boson masses the coupling $M\mu$ is very small for most of the

---

[6] During the writing of this paper, the BBH merger rate was updated based on GWTC-2 [17], $\mathcal{R}_{\mathrm{BBH}} = 23.9\ \mathrm{Gpc}^{-3}\ \mathrm{yr}^{-1}$. Although we do not use this new rate estimate in the search presented here, the update would not change the detectability of the signal model significantly, as the contribution from the BBH remnant population is mostly subdominant.

BHs in our population [see Eq. (2)] and, therefore, the total energy emitted in GWs over the lifetime of those BHs is typically much smaller for the scalar field case. In particular, for scalar fields with masses $m_b = 10^{-14}$ and $10^{-13.5}$ eV, the typical GW power for the systems in our BH population models is so small that the background spectra do not even appear in Fig. 2.

In addition to the comparison between the scalar and vector cloud models, Fig. 2 also shows a significant difference between the two BH formation channels. The spectra from the BBH merger remnant channel for vector boson masses $m_b \geq 10^{-11.5}$ eV are strongly suppressed, because such vector fields tend to induce strong superradiant instabilities only in lighter BHs ($M \lesssim 10\ \mathrm{M}_\odot$), which are less likely to be produced by this channel. In addition, one can notice from Fig. 2 that, for $m_b = 10^{-14}$ eV, the background due to the BBH remnant channel predicts a higher amplitude compared to the background induced by the isolated BH channel. This is to be contrasted with what happens for heavier vector bosons, where the opposite is true. This can be explained from the fact that the BHs formed through the isolated BH channel [typically $\mathcal{O}(10\ \mathrm{M}_\odot)$] are on average much lighter than the ones formed through the BBH merger remnant channel [typically $\sim\mathcal{O}(50\ \mathrm{M}_\odot)$ or more], such that for $m_b = 10^{-14}$ eV the GW emission timescale is typically much larger for the isolated BH channel compared to the BBH merger remnant channel [see Eq. (9)]. Therefore, for this boson mass, BBH merger remnants tend to radiate more energy within the lifetime of the BHs, leading to the strong suppression of the overall amplitude for the isolated channel with respect to the merger remnant channel that we see in Fig. 2. This hierarchical flip between the two BH formation channels also occurs in the scalar field case but occurs at $m_b \sim 10^{-13}$ eV due to the larger emission timescale for scalar fields (see Ref. [39]).

Lastly, in Fig. 3, we study how astrophysical uncertainties related to the choice of the BH population models impact the SGWB spectra. More specifically, while the BH mass function and local BBH merger rate we adopt are motivated by the theoretical and observational constraints as described in Ref. [39], there are currently several models for the cosmic star formation rate (SFR). Figure 3 shows how the energy density spectra change assuming four different SFR models: Hopkins and Beacom [98] (blue line), Wilkins, Trentham, and Hopkins [99] (yellow line), and two models from Vangioni *et al.* [100] (green and red lines). Vangioni *et al.* 2015 A/B represent different ways of calibrating the nominal SFR function. Model A calibrates it to the observational rate of gamma-ray bursts [101], whereas model B calibrates it to observations of the luminous galaxies [102,103]. We note that our BH population modeling implicitly assumes the SFR model of Vangioni *et al.* 2015 A. The contributions from both the isolated BH and BBH remnant channels are included under the assumption of isolated BH spin uniformly distributed over $\chi \in [0, 1]$. We find that over the boson mass range of interest, 10^{-13} to 10^{-12} eV, the uncertainties in the SFR would bring an astrophysical uncertainty of approximately a factor of 10 or less. This is typically much smaller than the uncertainty related to the unknown BH spin distribution. The SGWB spectrum predicted with the SFR model of Vangioni *et al.* 2015 A lies between the other SFR models, and, thus, the model we use in our analysis can be considered an intermediate scenario given the astrophysical uncertainty.

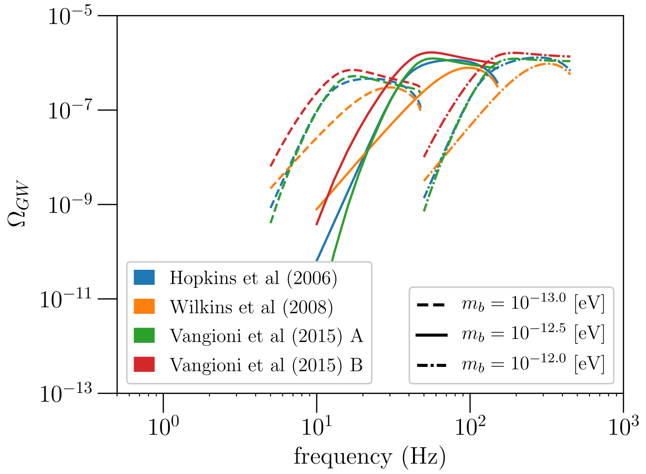

FIG. 3. Energy density spectra assuming different SFR models. Here, we adopt the following four SFR models: Hopkins and Beacom [98] (blue line), Wilkins, Trentham, and Hopkins [99] (yellow line), and two models from Vangioni *et al.* [100] (green and red lines). Vangioni *et al.* 2015 A/B represent different ways of calibrating the nominal SFR function; i.e., model A calibrates it to the observational rate of gamma-ray bursts [101], and model B calibrates it to observations of luminous galaxies [102,103]. The different line styles indicate the three vector masses, 10^{-13} to 10^{-12} eV. The contributions from both BH populations (isolated and merger remnant) are included under the assumption that the isolated BHs' spins are uniformly distributed over $\chi \in [0, 1]$.

D. Impact of modes with $m > 1$

The results shown above take into account only the mode with the smallest instability timescale, i.e., $m = 1$. However, the superradiant instability occurs for any azimuthal number m, as long as the superradiance condition Eq. (1) is satisfied. For some values of the boson mass and BH parameters, this condition will be satisfied only for $m > 1$ (either due to the BH's properties at birth or because the BH has been spun down by the $m = 1$ mode growing to saturation), making these modes relevant. As can be seen from Eqs. (13) and (16), the instability and GW emission timescales increase with m, and, therefore, in general, we expect the dominant contribution to the background to come from the most unstable mode $m = 1$. For the SGWB from ultralight scalar bosons, since the most unstable mode already has a typically long GW emission timescale, the contribution of higher modes to the total $\Omega_{\rm GW}(f)$ is, in general, much smaller, and, therefore, the contribution from these modes was not considered in Refs. [38,39]. Ultralight vector bosons, on the other hand, exhibit much smaller instability timescales, and, therefore, one might expect that the contribution from $m > 1$ modes could be important.

To study the impact of modes with $m > 1$, in Fig. 4, we compare the background produced by the $m = 1$ (solid lines) and $m = 2$ (dashed lines) modes, considering only the isolated BH channel, and assuming a uniform distribution $\chi \in [0, 0.8]$ for the natal BH spin. For this BH population, one can see that the contribution from the $m = 2$ mode is generally small for $m_b \lesssim 10^{-12}$ eV but can be as important as, or even dominate over, the contribution from the $m = 1$ mode for $m_b \gtrsim 10^{-12}$ eV. To understand why this happens, we note that, for a given BH mass and mode m, the critical BH spin below which a given mode is stable [Eq. (6)] increases with the boson mass, whereas for a fixed $M\mu$ it decreases with m. For example, for $m_b \sim 10^{-11}$ eV, a majority of the BH population is unstable only against $m > 1$ modes. For the few BHs that spin sufficiently fast to be unstable against the $m = 1$ mode, their natal spin is close to the critical spin, and, hence, much less energy is extracted and emitted by the $m = 1$ mode compared to the $m = 2$ mode.

We note, however, that, in the band where LIGO is most sensitive, the $m = 1$ contribution is, in general, dominant (see Fig. 4), and the contribution from the $m > 2$ modes is expected to be much smaller. Therefore, we will include only the contribution of the $m = 1$ and $m = 2$ modes in the signal model used in Secs. V and VII, where we show the results of injection studies and a search of this signal in Advanced LIGO's data.

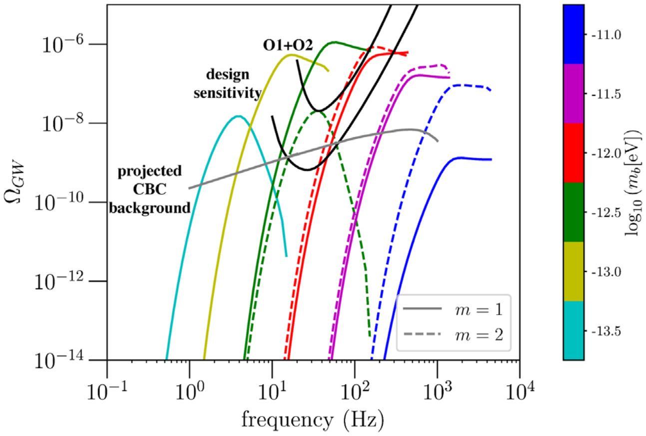

FIG. 4. Contribution to the energy density spectra of different m modes. The solid curves show the contribution from the $m = 1$ mode for the isolated BH model, whereas the dashed curves represent the contribution from the $m = 2$ mode. For the BH spin, we assume a uniform distribution $\chi \in [0, 0.8]$. The black solid curves are the (2σ) power-law integrated sensitivity curves [104], obtained using LIGO's first (O1) and second (O2) observing runs [36], and for Advanced LIGO at design sensitivity [105]. For comparison, we also show the predicted CBC background [37] (gray solid curve), which is extrapolated down to 1 Hz using a power-law spectrum model.

IV. SEARCH METHOD

In this section, we review the conventional search method and Bayesian statistics framework we use in order to either claim a detection or to place constraints on the SGWB model we presented above, when searching for such a background in LIGO data.

A. Definitions

For a single baseline with a pair of detectors, the SGWB is analyzed using the cross-correlation between two output streams. Although the formalism can be extended to handle a larger network of detectors [106,107], we will consider this simpler case as we analyze only the data from the two LIGO detectors. Following the notation in Ref. [108], we define a cross-correlation estimator that is optimal for a Gaussian background as [107,109]

$$\hat{C}(f) \equiv \frac{f^3}{T}\frac{20\pi^2}{3H_0^2}\tilde{s}_1^*(f)\tilde{s}_2(f). \tag{26}$$

Here, $\tilde{s}_i(f)$ is the Fourier transform of the time series output of the ith detector, T is the total observation time, and H_0 is the Hubble parameter. This is normalized such that

$$\langle\hat{C}(f)\rangle = \gamma(f)\Omega_{\rm GW}(f), \tag{27}$$

where $\gamma(f)$ is the overlap reduction function [110]. In the low signal-to-noise ratio limit, the variance of the cross-correlation estimator $\hat{C}(f)$ is approximately given by

$$\sigma^2(f) \approx \frac{1}{2T\Delta f}\left(\frac{10\pi^2 f^3}{3H_0^2}\right)^2 P_1(f)P_2(f), \tag{28}$$

where Δf is the frequency resolution and $P_i(f)$ is the power spectral density (PSD) of the ith detector.

B. Bayesian inference

Following the method in Ref. [111], we discuss a Bayesian formalism for our detection statistics, parameter estimation, and model selection. For our analysis, Bayes' theorem states that, using the estimator $\hat{C}(f)$,

$$p(\boldsymbol{\theta}_{\mathcal{A}}|\{\hat{C}\},\mathcal{A}) = \frac{L(\{\hat{C}\}|\boldsymbol{\theta}_{\mathcal{A}},\mathcal{A})\pi(\boldsymbol{\theta}_{\mathcal{A}}|\mathcal{A})}{Z(\{\hat{C}\}|\mathcal{A})}, \tag{29}$$

where $p(\boldsymbol{\theta}_{\mathcal{A}}|\{\hat{C}\},\mathcal{A})$ is the posterior probability on the multidimensional space of parameters $\boldsymbol{\theta}_{\mathcal{A}}$ that describe the

SGWB model in the signal hypothesis $\mathcal{A}$, $L(\{\hat{C}\}|\boldsymbol{\theta}_{\mathcal{A}}, \mathcal{A})$ is the likelihood, $\pi(\boldsymbol{\theta}_{\mathcal{A}}|\mathcal{A})$ is the prior probability of the parameters $\boldsymbol{\theta}_{\mathcal{A}}$, and $Z(\{\hat{C}\}|\mathcal{A})$ is the evidence. We use nested sampling package PyMultiNest [112] to evaluate the likelihood. PyMultiNest is a PYTHON interface to the nested sampling package MultiNest [113–115], which produces a set of samples drawn from an estimated posterior.

Let $\{\hat{C}\}$ be the cross-correlation estimator obtained from the data within an analyzed frequency band. For a given $\{\hat{C}\}$, we define a Gaussian likelihood for every frequency bin, and, hence, a joint likelihood given by the product of each likelihood, such that

$$\begin{aligned}\ln[L(\{\hat{C}\}|\boldsymbol{\theta}_{\mathcal{A}}, \mathcal{A})] &= \sum_f \ln[L(\hat{C}(f)|\boldsymbol{\theta}_{\mathcal{A}}, \mathcal{A})] \\ &= \sum_f \left\{-\frac{[\hat{C}(f) - \gamma(f)\Omega_{\mathcal{A}}(f;\boldsymbol{\theta}_{\mathcal{A}})]^2}{2\sigma^2(f)} - \frac{1}{2}\ln(2\pi\sigma^2(f))\right\}.\end{aligned} \tag{30}$$

Here, $\Omega_{\mathcal{A}}(f;\boldsymbol{\theta}_{\mathcal{A}})$ is a model energy-density spectrum for a given set of parameters $\boldsymbol{\theta}_{\mathcal{A}}$.

For the priors, we set a log-uniform prior[7] on the vector mass m_b and a linearly uniform prior on the BH spin upper and lower limits $\chi_{\mathrm{ul/ll}}$. Therefore, following Bayes' theorem [Eq. (29)], the posterior probability is inversely proportional to the boson mass:

$$p(\boldsymbol{\theta}_{\mathcal{A}}|\{\hat{C}\}, \mathcal{A}) \propto \frac{1}{m_b} L(\{\hat{C}\}|\boldsymbol{\theta}_{\mathcal{A}}, \mathcal{A}). \tag{31}$$

We will also be interested in performing model selection between different signal models. The Bayesian evidence for a given hypothesis quantifies how well the model fits the obtained data and is defined as

$$Z(\{\hat{C}\}|\mathcal{A}) = \int L(\{\hat{C}\}|\boldsymbol{\theta}_{\mathcal{A}}, \mathcal{A})\pi(\boldsymbol{\theta}_{\mathcal{A}}|\mathcal{A})\mathrm{d}^D\boldsymbol{\theta}_{\mathcal{A}}. \tag{32}$$

This expression can also be interpreted as the fully marginalized likelihood over the entire parameter space. In the case where no signal is present (the null hypothesis), the evidence is obtained by fixing $\Omega_{\mathcal{A}}(f;\theta_{\mathcal{A}})$ to zero in the likelihood [Eq. (30)]. To assess which hypothesis, $\mathcal{A}$ or $\mathcal{B}$, better describes the observed data, we can compute the odds ratio $\mathcal{O}^{\mathcal{A}}_{\mathcal{B}}$ defined as

$$\mathcal{O}^{\mathcal{A}}_{\mathcal{B}} \equiv \frac{p(\mathcal{A}|\{\hat{C}\})}{p(\mathcal{B}|\{\hat{C}\})} = \frac{Z(\{\hat{C}\}|\mathcal{A})}{Z(\{\hat{C}\}|\mathcal{B})}\frac{\pi(\mathcal{A})}{\pi(\mathcal{B})}, \tag{33}$$

where $Z(\{\hat{C}\}|\mathcal{A})$ and $Z(\{\hat{C}\}|\mathcal{B})$ are the evidence for the hypotheses $\mathcal{A}$ and $\mathcal{B}$, respectively, whereas $\pi(\mathcal{A})$ and $\pi(\mathcal{B})$ are the prior probability of the respective hypothesis. Hereafter, we will set the *a priori* probability ratio for the two models, $\pi(\mathcal{A})/\pi(\mathcal{B})$, to unity. Therefore, for our case, the odds ratio will be effectively equivalent to the Bayes factor (defined as the ratio between the evidences). In what follows, we will evaluate the statistical significance for a given hypothesis in terms of the Bayes factor and follow the convention that a natural logarithmic Bayes factor ≈ 8 indicates that one model is favored over the other with great confidence [117].

V. RESULTS

We are now in a position to study the sensitivity of Advanced LIGO to the SGWB we described in Sec. III, using the tools introduced in the previous section. We first study the range of vector boson masses that LIGO will be able to probe at its design sensitivity by performing injections of the SGWB model into synthesized data and then explore if one could successfully discriminate between the SGWB due to CBCs and the one due to the superradiant instability.

A. Range of sensitivity for vector boson masses

The results shown in Fig. 4 suggest that, for vector bosons with masses roughly in the range $m_b \sim [10^{-13}, 10^{-12}]$ eV, the SGWB could be detected by LIGO at design sensitivity and that even with the sensitivity of LIGO's first and second observing runs, one could already probe bosons with masses $m_b \sim 10^{-12.5}$ eV. To study this in more detail and assess the vector mass range that we can probe through this method, we inject our SGWB model into synthesized data with different values of the model parameters and then infer the detectability of the signal by computing Bayes factors between the signal and noise hypotheses.

We follow the injection scheme described in Ref. [39], where the simulated cross-correlation spectrum is defined as

$$\hat{C}_{\mathrm{sim}}(f) \equiv \gamma_{\mathrm{HL}}(f)\Omega_{\mathrm{inj}}(f;\boldsymbol{\theta}_{\mathrm{inj}}) + \sigma(f)\hat{n}. \tag{34}$$

Here, $\gamma_{\mathrm{HL}}(f)$ is the overlap reduction function for the LIGO baseline [110], $\Omega_{\mathrm{inj}}(f;\boldsymbol{\theta}_{\mathrm{inj}})$ is the injected background for the given model parameters $\boldsymbol{\theta}_{\mathrm{inj}}$, and $\hat{n}$ is a random variable drawn from a Gaussian distribution with zero mean and unit variance. To synthesize data, we set Δf as 0.25 Hz for the injection studies in this and the next subsections and specify $\sigma(f)$ using Eq. (28) for a given PSD and observation time. We assume 3 yr of observation with the projected design sensitivity PSD for the LIGO

---

[7] At this point, we choose to adopt mostly uninformative priors for $\boldsymbol{\theta}_{\mathcal{A}}$, since this is the most conservative choice. However, in principle, we could also choose a prior that encodes prior knowledge on the boson mass obtained from independent experiments, such as constraints from BH spin measurements in x-ray binaries [54,55,61,116]. This will be revisited in future work.

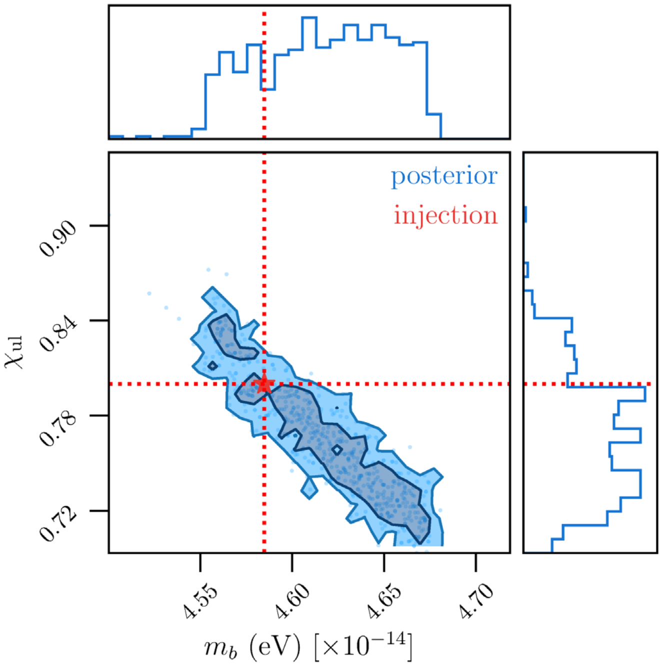

FIG. 5. The posterior samples recovered for one of the injections $\Omega_{\rm inj}(f;\boldsymbol{\theta})$ where the injected parameters $\boldsymbol{\theta}_{\rm inj}$ are $(m_b, \chi_{\rm ul}) = (4.58 \times 10^{-14}\ {\rm eV}, 0.8)$ and $\chi_{\rm ll} = 0$ is kept fixed in the parameter recovery. The star marker indicates the true values for the injected parameters. The contours represent the 2 and 3σ credible regions.

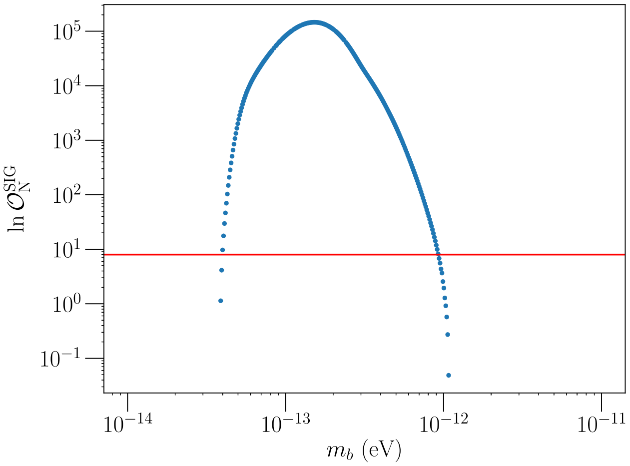

FIG. 6. The Bayes factor of the recovered signal as a function of injected m_b[eV], fixing $\chi_{\rm ll} = 0$ and $\chi_{\rm ul} = 0.8$ in the injected signals. The red horizontal line shows our detection criterion $\ln \mathcal{O}^{\rm SIG}_{\rm N} = 8$. Injections that have a Bayes factor above the red line are confidently detected.

detectors [105] (see Fig. 4). From this simulated cross-correlation spectrum, our pipeline computes the likelihood function and the posterior distribution of the parameters $\boldsymbol{\theta}_{\rm inj}$, as well as the Bayesian evidence $Z(\{C_{\rm inj}\})$.

In Fig. 5, we show an example of the parameter estimation results for one of the injections, where the injected parameters $\boldsymbol{\theta}_{\rm inj}$ are $m_b = 4.58 \times 10^{-14}$ eV and $(\chi_{\rm ul}, \chi_{\rm ll}) = (0.8, 0)$. In the parameter estimation recovery, we adopt the more conservative parametrization for $p(\chi)$ where $\chi_{\rm ll} = 0$ is kept fixed while $\chi_{\rm ul}$ is allowed to vary. In order to obtain evidence for the noise hypothesis, we also perform the same analysis for the identical noise realization without the injection. The star marker represents the true parameters of the injection, which lie within the 2 and 3σ contours. For this recovered injection, we estimate the signal-to-noise ratio to be 20.2 and find that the log Bayes factor of the signal versus noise hypotheses is approximately 500, showing that the signal is detected with great confidence.

We repeat this injection recovery varying the vector boson mass of each injection but using the same BH spin distribution for all injections, namely, a uniform distribution with $\chi_{\rm ll} = 0$ and $\chi_{\rm ul} = 0.8$ [see Eq. (21)]. Our results are summarized in Fig. 6, where we show the log Bayes factor as a function of the vector boson mass for this set of injections. These results indicate that, given the detection criteria of $\ln \mathcal{O}^{\rm SIG}_{\rm N} = 8$, we could detect vector bosons with masses in the range 5×10^{-14} to 10^{-12} eV. We note that this detectable mass range is wider than that for ultralight scalar bosons due to the enhanced energy spectrum for masses below $m_b \lesssim 10^{-13}$ eV (cf. Fig. 5 in Ref. [39]).

B. Distinguishing the background from vector clouds and CBCs

In the previous subsection, we neglected the fact that, besides the SGWB signal due to the formation of vector clouds, CBCs also produce a background that is expected to be detectable by Advanced LIGO at design sensitivity, and so in reality we should consider *both* types of SGWBs in our simulation. Figure 4 illustrates that the SGWB signal from the vector clouds can dominate over the projected CBC background for some choices of the vector mass and BH spin distribution, and, therefore, a natural question to ask is whether we can distinguish between these two signal models based on the Bayesian framework of Sec. V B. A similar study was done in Ref. [39] for the case of scalar boson clouds, and here we repeat this study for the vector boson model.

We consider an energy density spectrum that consists of the contributions from both the vector cloud and the projected CBC background, which reads

$$\Omega_{\rm inj}(f;\boldsymbol{\theta}) = \Omega^{\rm VC}_{\rm inj}(f;\boldsymbol{\theta}) + \Omega^{\rm CBC}_{\rm inj}(f). \qquad (35)$$

$\Omega^{\rm VC}_{\rm inj}(f;\boldsymbol{\theta})$ is the background due to superradiant instabilities under a $\chi_{\rm ul}$ parametrization of the natal spin distribution for isolated BHs [Eq. (25)], and $\Omega^{\rm CBC}_{\rm inj}(f)$ is the fixed CBC background approximated as a power-law spectrum:

$$\Omega_{\rm GW}^{\rm CBC}(f) = 1.8 \times 10^{-9}\left(\frac{f}{25\ {\rm Hz}}\right)^{2/3}, \tag{36}$$

as inferred from Ref. [37].

Because of the computational expense, for the injection recovery of the vector cloud background, we consider only the isolated BH channel [Eq. (20)]. Since the merger remnant channel is subdominant for the boson masses of interest (see Fig. 2) and slightly below the projected CBC background, we do not expect the inclusion of this additional channel to change the results significantly. Like we did in the previous subsection, we adopt the $\chi_{\rm ul}$ parametrization for $p(\chi)$; i.e., we use a parametrization where $\chi_{\rm ll} = 0$ is kept fixed while $\chi_{\rm ul}$ is allowed to vary. The injected CBC background is recovered with the following parametrization[8]:

$$\Omega_{\rm rec}^{\rm CBC}(f;\Omega_0,\alpha) \equiv \Omega_0\left(\frac{f}{25\ {\rm Hz}}\right)^{\alpha}. \tag{37}$$

To see whether we can detect the vector cloud background in the presence of the CBC background, we will compute a log Bayes factor between two hypotheses: a CBC-only hypothesis, corresponding to the hypothesis that only the CBC background is present in the data, and a joint vector cloud and CBC hypothesis (VC + CBC), corresponding to the hypothesis that both the CBC and vector cloud backgrounds are present in the data. The parameters considered when evaluating the evidence for each background model are listed in Table III. We repeat this computation for several injections, varying the parameters $(m_b, \chi_{\rm ul})$ until we explore a grid over the entire prior space. The results of this study are shown in Fig. 7, where we plot a grayscale map of the log Bayes factors, highlighting the contours where $\ln \mathcal{O}_{\rm CBC}^{\rm VC+CBC} = 8$ (magenta contour) and $\ln \mathcal{O}_{\rm CBC}^{\rm VC+CBC} = 0$ (cyan contour). The parameter space inside the magenta contour indicates the region where one can confidently discern the vector cloud background from the projected CBC background. As expected, for large $\chi_{\rm ul}$ the range of boson masses for which one could claim a confident detection agrees with the one obtained in the previous subsection.

TABLE III. Parameters in each recovered background model.

Models	CBC-only	VC + CBC
Parameters	Ω_0, α	$m_b, \chi_{\rm ul}, \Omega_0, \alpha$

VI. CONSTRAINTS ON ULTRALIGHT VECTOR BOSONS USING LIGO DATA

Using the Bayesian framework presented in Sec. IV, we now conduct a search for the vector cloud background [Eq. (18)] using the cross-correlation spectra obtained from the first (O1) and second (O2) observing runs of Advanced LIGO [36]. (The data products used in this paper are publicly available at Ref. [120].) The analysis is conducted following the prescription presented in the injection studies done in Secs. V A and V B, except for the likelihood evaluation. Since in this case the independent cross-correlation spectrum is obtained from each observing run, the full likelihood expression takes the form

$$L(\hat{C}_{\rm O1}, \hat{C}_{\rm O2}|\boldsymbol{\theta}, \mathcal{H}_{\rm VC}) = L(\hat{C}_{\rm O1}|\boldsymbol{\theta}, \mathcal{H}_{\rm VC})L(\hat{C}_{\rm O2}|\boldsymbol{\theta}, \mathcal{H}_{\rm VC}), \tag{38}$$

where each likelihood in the right-hand side follows the definition of Eq. (30). These cross-correlation spectra are provided over the frequency range from 20 to 700 Hz with the frequency resolution of $\Delta f = 1/32$ Hz.

We do not find statistically significant evidence for a vector cloud background. Therefore, we place constraints on the two-dimensional space $(m_b, \chi_{\rm ul,ll})$ using the estimated posterior probability distribution. Figures 8 and 9 show the posteriors under the $\chi_{\rm ul}$ and $\chi_{\rm ll}$ parametrizations, respectively [see Eq. (21) and the corresponding discussion]. In particular, the results shown in Fig. 8 indicate that, when using the $\chi_{\rm ul}$ parametrization, the data disfavor boson masses close to $m_b \approx 10^{-13}$ eV and relatively high $\chi_{\rm ul} \gtrsim 0.2$. We note, however, that the marginalized 1D posterior for m_b does not indicate a strong constraint at the

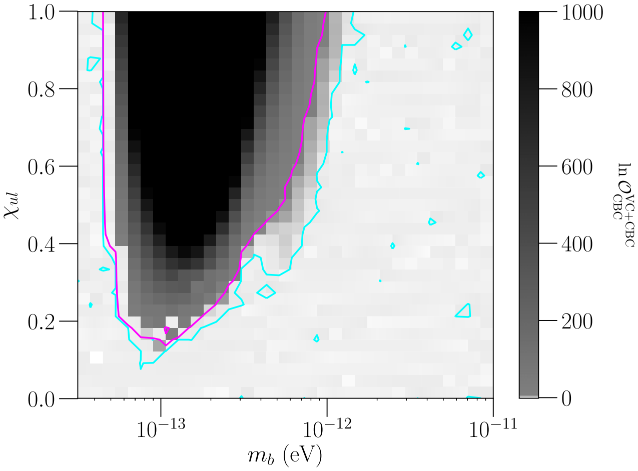

FIG. 7. Grayscale map of a log Bayes factor between CBC-only and the joint VC + CBC models with two contours of $\ln \mathcal{O}_{\rm CBC}^{\rm VC+CBC} = 8$ (magenta curve) and 0 (cyan curve). The parameter space inside the magenta contour indicates the region where one can confidently discern the vector cloud background from the projected CBC background.

---

[8] We refer to Eq. (37) as a CBC model, even though this could be generally called a "power-law spectrum model." It has been shown that the systematic error potentially caused by this bias is below the statistical error and, hence, would not affect the detectability of the background [118,119].

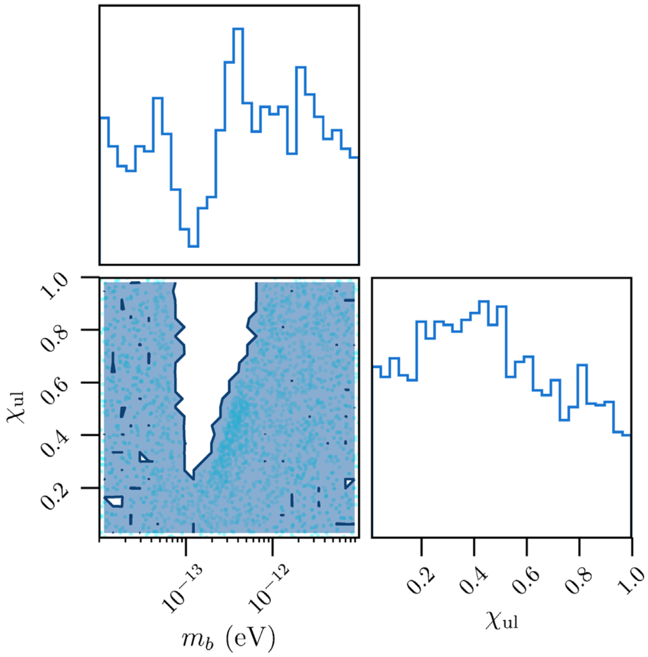

FIG. 8. Posterior results obtained with the data from the first and second observing runs of Advanced LIGO, recovered with the $\chi_{\rm ul}$ parameterization. The contour on the two-dimensional posterior represents the 95% confidence level.

95% confidence level. On the other hand, when we fix $\chi_{\rm ul} = 1$ and allow the lower bound $\chi_{\rm ll}$ to vary, then Fig. 9 suggests that the mass range 0.8×10^{-13} to 6.5×10^{-13} eV is excluded (95% credible interval) regardless of the spin's lower bound $\chi_{\rm ll}$, as can be seen in the 1D marginalized posterior of m_b.

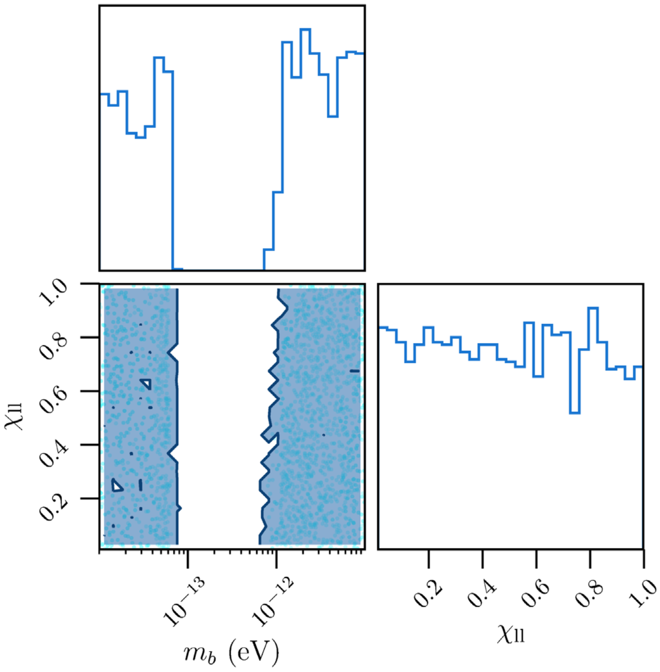

FIG. 9. Posterior results, analogous to Fig. 8, for the $\chi_{\rm ll}$ spin parameterization.

In summary, these results suggest that minimally coupled vector bosons with masses around $m_b \approx 10^{-13}$ eV are highly disfavored, unless most stellar-mass BHs are born with a small spin.

VII. CONCLUSION

In this paper, we computed and studied in detail the SGWB produced by the superposition of GW signals from extragalactic BH-ultralight vector cloud systems formed through the superradiant instability. Using a Bayesian framework, we performed the first search for such signal in LIGO data. This extends previous works [38,39] where a similar background for scalar bosons was studied. We also improved on those works by adding the contribution of the second most unstable mode, $m = 2$ (in addition to the most unstable one, $m = 1$), to the SGWB model, which was not considered in Refs. [38,39]. In particular, we found that the contribution from the $m = 2$ mode can be as important as, or even dominate over, the $m = 1$ mode for $m_b \geq 10^{-12}$ eV and, therefore, affect the detectability and potential constraints on the vector boson mass.

To estimate the potential detectable window, we performed injection tests on simulated Advanced LIGO data at design sensitivity and found that Advanced LIGO is especially sensitive to the background emitted by minimally coupled vector bosons with masses in the range $\sim[5 \times 10^{-14}, 10^{-12}]$ eV (see Fig. 6). This detectable mass range is broader than that for ultralight scalar bosons (cf. Fig. 5 in Ref. [39]), especially at small masses, due to the considerably larger GW power for vector bosons. We also studied the capability to claim a detection for this background model in the presence of a (fiducial) CBC background model. Our results suggest that we can distinguish between both models in a large part of the parameter space (see Fig. 7).

Additionally, in the future, we may be able to place constraints using only BBH merger remnants, which are much less sensitive to unknown BH population statistics. We performed similar simulations using the LIGO's design sensitivity with and without an injection to search for the BBH remnant component alone. With the injection of the SGWB for $m_b = 10^{-13}$ eV, we recovered it with a Bayes factor of 10.4 and consistent vector mass estimation. On the other hand, without the injection, we ruled out $m_b \sim 10^{-13}$ eV at the 95% confidence level. Although we leave the model selection test between this and the CBC background as future work, these results indicate that we will potentially be able to make a detection, or place more robust constraints on the vector mass, by probing the BBH remnant signal model.

Lastly, we presented results obtained by analyzing data from Advanced LIGO's first and second observing runs.

We did not find any signal consistent with our vector cloud model, independent of the parametrizations employed for the BH spin distribution. For the more optimistic parametrization (the $\chi_{\rm ul}$ parametrization), we rule out (minimally coupled) ultralight vector bosons in the mass range 0.8×10^{-13} to 6.5×10^{-13} eV with 95% percent credibility. A less optimistic parametrization $\chi_{\rm ll}$, which allows for the possibility that all isolated BHs have negligible spins, does not give strong constraints. However, boson masses around $\sim 10^{-13}$ eV are highly disfavored by our results, unless all isolated BHs form with spins $\lesssim 0.2$. We note that these constraints depend on our specific choice for the BH spin distribution as well as the astrophysical models we adopted in this analysis.

Aside from these constraints, the observation of stellar-mass BHs in x-ray binaries spinning above the superradiant threshold already disfavors the existence of ultralight vector fields in the range $\sim[10^{-14}, 10^{-11}]$ eV [54,55,61,116], which overlaps with the range of masses we are able to probe with the SGWB. However, we should note that such constraints should be interpreted with caution, since BH spin measurements from x-ray binaries are often susceptible to large systematic uncertainties (see, e.g., Ref. [121]). GW searches should, therefore, be seen as complementary to those measurements. Given sufficiently robust estimates of all the relevant uncertainties, it could be interesting to include GW searches and BH spin measurements in the same Bayesian framework, which would, in principle, lead to stronger constraints.

We considered only a minimally coupled ultralight vector field, neglecting possible (nongravitational) couplings with other particles, as well as any nontrivial self-interactions beyond the mass term. Our results apply to any massive vector field as long as any additional interactions are negligible compared to the gravitational interaction between the BH and vector field. Sufficiently large nongravitational interactions could change the picture, in particular, by affecting the evolution of the superradiant instability. For example, for ultralight scalar fields it has been shown that self-interactions [62,122,123] and couplings to photons [124–126] can quench the superradiant instability and effectively increase the timescale needed to extract a substantial amount of energy and angular momentum from the BH [127,128]. The effect of such interactions has been less studied for massive vector fields—with the exception of some consideration of the case where the vector boson mass arises through a Higgs mechanism [54,127]—but one might expect that similar results also apply for this case. It would be important to study this question in more detail in the future. Finally, we should note that if ultralight dark-matter photons couple directly to ordinary matter, they could also produce another kind of observable signal in GW interferometers by inducing displacements on the LIGO mirrors [129–132]. Since our results mainly apply to ultralight bosons for which nongravitational interactions are negligible, our constraints complement those searches.

ACKNOWLEDGMENTS

L. T. is also grateful for computational resources provided by the LIGO lab and supported by National Science Foundation Grants No. PHY-0757058 and No. PHY-0823459. L. T. is supported by JSPS KAKENHI Grant No. JP18J21709. N. S. thanks Masha Baryakhtar for useful discussions during the completion of this work. N. S. and W. E. E. acknowledge support from an NSERC Discovery grant. Research at Perimeter Institute is supported in part by the Government of Canada through the Department of Innovation, Science and Economic Development Canada and by the Province of Ontario through the Ministry of Colleges and Universities. R. B. acknowledges financial support from the European Union's Horizon 2020 research and innovation program under the Marie Skłodowska-Curie Grant Agreement No. 792862, from the European Union's H2020 ERC, Starting Grant Agreement No. DarkGRA-757480, and from the MIUR PRIN and FARE programs (GW-NEXT, CUP: B84I20000100001). This research was supported by the Amaldi Research Center funded by the MIUR program "Dipartimento di Eccellenza" (CUP: B81I18001170001).

[1] B. P. Abbott *et al.* (LIGO Scientific and Virgo Collaborations), Phys. Rev. Lett. **116**, 061102 (2016).

[2] B. P. Abbott *et al.* (LIGO Scientific and Virgo Collaborations), Phys. Rev. Lett. **116**, 241103 (2016).

[3] B. P. Abbott *et al.* (LIGO Scientific and Virgo Collaborations), Phys. Rev. X **6**, 041015 (2016).

[4] B. P. Abbott *et al.* (LIGO Scientific and Virgo Collaborations), Phys. Rev. Lett. **118**, 221101 (2017).

[5] B. P. Abbott *et al.* (LIGO Scientific and Virgo Collaborations), Astrophys. J. **851**, L35 (2017).

[6] B. P. Abbott *et al.* (LIGO Scientific and Virgo Collaborations), Phys. Rev. Lett. **119**, 141101 (2017).

[7] B. P. Abbott *et al.* (LIGO Scientific and Virgo Collaborations), Phys. Rev. Lett. **119**, 161101 (2017).

[8] B. P. Abbott *et al.* (LIGO Scientific and Virgo Collaborations), Phys. Rev. X **9**, 031040 (2019).

[9] R. Abbott *et al.* (LIGO Scientific and Virgo Collaborations), Phys. Rev. D **102**, 043015 (2020).

[10] B. Abbott *et al.* (LIGO Scientific and Virgo Collaborations), Astrophys. J. Lett. **892**, L3 (2020).

[11] R. Abbott *et al.* (LIGO Scientific and Virgo Collaborations), Astrophys. J. Lett. **896**, L44 (2020).
[12] R. Abbott *et al.* (LIGO Scientific and Virgo Collaborations), Phys. Rev. Lett. **125**, 101102 (2020).
[13] R. Abbott *et al.* (LIGO Scientific and Virgo Collaboration), arXiv:2010.14527.
[14] B. P. Abbott *et al.* (LIGO Scientific and Virgo Collaborations), Astrophys. J. **818**, L22 (2016).
[15] B. P. Abbott *et al.* (LIGO Scientific and Virgo Collaborations), Astrophys. J. Lett. **882**, L24 (2019).
[16] L. Barack *et al.*, Classical Quantum Gravity **36**, 143001 (2019).
[17] R. Abbott *et al.* (LIGO Scientific and Virgo Collaboration), arXiv:2010.14533.
[18] B. P. Abbott *et al.* (LIGO Scientific and Virgo Collaborations), Phys. Rev. Lett. **116**, 221101 (2016); **121**, 129902 (E) (2018).
[19] B. P. Abbott *et al.* (LIGO Scientific and Virgo Collaborations), Phys. Rev. Lett. **123**, 011102 (2019).
[20] B. P. Abbott *et al.* (LIGO Scientific and Virgo Collaborations), Phys. Rev. D **100**, 104036 (2019).
[21] G. Bertone *et al.*, SciPost Phys. Core **3**, 007 (2020).
[22] R. Abbott *et al.* (LIGO Scientific and Virgo Collaboration), arXiv:2010.14529.
[23] J. Calderón Bustillo, N. Sanchis-Gual, A. Torres-Forné, J. A. Font, A. Vajpeyi, R. Smith, C. Herdeiro, E. Radu, and S. H. Leong, Phys. Rev. Lett. **126**, 081101 (2021).
[24] B. P. Abbott *et al.* (KAGRA, LIGO Scientific, and Virgo Collaborations), Living Rev. Relativity **21**, 3 (2018).
[25] J. Aasi *et al.* (LIGO Scientific Collaboration), Classical Quantum Gravity **32**, 074001 (2015).
[26] F. Acernese *et al.* (Virgo Collaboration), Classical Quantum Gravity **32**, 024001 (2015).
[27] Y. Aso, Y. Michimura, K. Somiya, M. Ando, O. Miyakawa, T. Sekiguchi, D. Tatsumi, and H. Yamamoto (KAGRA Collaboration), Phys. Rev. D **88**, 043007 (2013).
[28] B. Iyer *et al.*, https://dcc.ligo.org/LIGO-M1100296/public (2011).
[29] M. Maggiore *et al.*, J. Cosmol. Astropart. Phys. 03 (2020) 050.
[30] D. Reitze *et al.*, Bull. Am. Astron. Soc. **51**, 035 (2019).
[31] P. Amaro-Seoane *et al.* (LISA Collaboration), arXiv:1702.00786.
[32] B. Perera *et al.*, Mon. Not. R. Astron. Soc. **490**, 4666 (2019).
[33] N. Christensen, Rep. Prog. Phys. **82**, 016903 (2019).
[34] B. P. Abbott *et al.* (LIGO Scientific and Virgo Collaborations), Phys. Rev. Lett. **116**, 131102 (2016).
[35] B. P. Abbott *et al.* (LIGO Scientific and Virgo Collaborations), Phys. Rev. Lett. **118**, 121101 (2017).
[36] B. P. Abbott *et al.* (LIGO Scientific and Virgo Collaborations), Phys. Rev. D **100**, 061101 (2019).
[37] B. P. Abbott *et al.* (LIGO Scientific and Virgo Collaborations), Phys. Rev. Lett. **120**, 091101 (2018).
[38] R. Brito, S. Ghosh, E. Barausse, E. Berti, V. Cardoso, I. Dvorkin, A. Klein, and P. Pani, Phys. Rev. Lett. **119**, 131101 (2017).
[39] L. Tsukada, T. Callister, A. Matas, and P. Meyers, Phys. Rev. D **99**, 103015 (2019).
[40] X.-L. Fan and Y. Chen, Phys. Rev. D **98**, 044020 (2018).
[41] T. Damour, N. Deruelle, and R. Ruffini, Lett. Nuovo Cimento **15**, 257 (1976).
[42] T. Zouros and D. Eardley, Ann. Phys. (N.Y.) **118**, 139 (1979).
[43] S. L. Detweiler, Phys. Rev. D **22**, 2323 (1980).
[44] S. R. Dolan, Phys. Rev. D **76**, 084001 (2007).
[45] A. Arvanitaki, S. Dimopoulos, S. Dubovsky, N. Kaloper, and J. March-Russell, Phys. Rev. D **81**, 123530 (2010).
[46] Y. Shlapentokh-Rothman, Commun. Math. Phys. **329**, 859 (2014).
[47] P. Pani, V. Cardoso, L. Gualtieri, E. Berti, and A. Ishibashi, Phys. Rev. Lett. **109**, 131102 (2012).
[48] P. Pani, V. Cardoso, L. Gualtieri, E. Berti, and A. Ishibashi, Phys. Rev. D **86**, 104017 (2012).
[49] H. Witek, V. Cardoso, A. Ishibashi, and U. Sperhake, Phys. Rev. D **87**, 043513 (2013).
[50] R. Brito, V. Cardoso, and P. Pani, Phys. Rev. D **88**, 023514 (2013).
[51] S. Endlich and R. Penco, J. High Energy Phys. 05 (2017) 052.
[52] W. E. East, Phys. Rev. D **96**, 024004 (2017).
[53] W. E. East and F. Pretorius, Phys. Rev. Lett. **119**, 041101 (2017).
[54] M. Baryakhtar, R. Lasenby, and M. Teo, Phys. Rev. D **96**, 035019 (2017).
[55] V. Cardoso, Ó. J. Dias, G. S. Hartnett, M. Middleton, P. Pani, and J. E. Santos, J. Cosmol. Astropart. Phys. 03 (2018) 043.
[56] W. E. East, Phys. Rev. Lett. **121**, 131104 (2018).
[57] V. P. Frolov, P. Krtouš, D. Kubizňák, and J. E. Santos, Phys. Rev. Lett. **120**, 231103 (2018).
[58] S. R. Dolan, Phys. Rev. D **98**, 104006 (2018).
[59] D. Baumann, H. S. Chia, J. Stout, and L. ter Haar, J. Cosmol. Astropart. Phys. 12 (2019) 006.
[60] R. Brito, S. Grillo, and P. Pani, Phys. Rev. Lett. **124**, 211101 (2020).
[61] R. Brito, V. Cardoso, and P. Pani, *Superradiance: New Frontiers in Black Hole Physics* (Springer, New York, 2020), Vol. 971.
[62] A. Arvanitaki and S. Dubovsky, Phys. Rev. D **83**, 044026 (2011).
[63] A. Arvanitaki, M. Baryakhtar, and X. Huang, Phys. Rev. D **91**, 084011 (2015).
[64] A. Arvanitaki, M. Baryakhtar, S. Dimopoulos, S. Dubovsky, and R. Lasenby, Phys. Rev. D **95**, 043001 (2017).
[65] R. Brito, S. Ghosh, E. Barausse, E. Berti, V. Cardoso, I. Dvorkin, A. Klein, and P. Pani, Phys. Rev. D **96**, 064050 (2017).
[66] S. D’Antonio, C. Palomba, P. Astone, S. Frasca, G. Intini, I. La Rosa, P. Leaci, S. Mastrogiovanni, A. Miller, F. Muciaccia, O. J. Piccinni, and A. Singhal, Phys. Rev. D **98**, 103017 (2018).
[67] C. Palomba, S. D’Antonio, P. Astone, S. Frasca, G. Intini, I. La Rosa, P. Leaci, S. Mastrogiovanni, A. L. Miller, F. Muciaccia, O. J. Piccinni, L. Rei, and F. Simula, Phys. Rev. Lett. **123**, 171101 (2019).
[68] M. Isi, L. Sun, R. Brito, and A. Melatos, Phys. Rev. D **99**, 084042 (2019).
[69] S. Ghosh, E. Berti, R. Brito, and M. Richartz, Phys. Rev. D **99**, 104030 (2019).

[70] L. Sun, R. Brito, and M. Isi, Phys. Rev. D **101**, 063020 (2020).
[71] S. J. Zhu, M. Baryakhtar, M. A. Papa, D. Tsuna, N. Kawanaka, and H.-B. Eggenstein, Phys. Rev. D **102**, 063020 (2020).
[72] R. Essig *et al.*, arXiv:1311.0029.
[73] D. J. E. Marsh, Phys. Rep. **643**, 1 (2016).
[74] L. Hui, J. P. Ostriker, S. Tremaine, and E. Witten, Phys. Rev. D **95**, 043541 (2017).
[75] I. G. Irastorza and J. Redondo, Prog. Part. Nucl. Phys. **102**, 89 (2018).
[76] M. Baldeschi, R. Ruffini, and G. Gelmini, Phys. Lett. **122B**, 221 (1983).
[77] M. Goodsell, J. Jaeckel, J. Redondo, and A. Ringwald, J. High Energy Phys. 11 (2009) 027.
[78] J. Jaeckel and A. Ringwald, Annu. Rev. Nucl. Part. Sci. **60**, 405 (2010).
[79] P. W. Graham, J. Mardon, and S. Rajendran, Phys. Rev. D **93**, 103520 (2016).
[80] P. Agrawal, N. Kitajima, M. Reece, T. Sekiguchi, and F. Takahashi, Phys. Lett. B **801**, 135136 (2020).
[81] R. Peccei and H. R. Quinn, Phys. Rev. Lett. **38**, 1440 (1977).
[82] S. Weinberg, Phys. Rev. Lett. **40**, 223 (1978).
[83] R. T. Co, A. Pierce, Z. Zhang, and Y. Zhao, Phys. Rev. D **99**, 075002 (2019).
[84] Y. Nakai, R. Namba, and Z. Wang, J. High Energy Phys. 12 (2020) 170.
[85] R. Namba and M. Suzuki, Phys. Rev. D **102**, 123527 (2020).
[86] N. Siemonsen and W. E. East, Phys. Rev. D **101**, 024019 (2020).
[87] H. Yoshino and H. Kodama, Prog. Theor. Phys. **2014**, 043E02 (2014).
[88] R. Brito, V. Cardoso, and P. Pani, Classical Quantum Gravity **32**, 134001 (2015).
[89] C. A. R. Herdeiro and E. Radu, Phys. Rev. Lett. **119**, 261101 (2017).
[90] O. Lunin, J. High Energy Phys. 12 (2017) 138.
[91] S. A. Teukolsky, Astrophys. J. **185**, 635 (1973).
[92] P. Krtouš, V. P. Frolov, and D. Kubizňák, Nucl. Phys. **B934**, 7 (2018).
[93] E. Phinney, arXiv:astro-ph/0108028.
[94] P. B. Covas *et al.* (LSC Instrument Authors), Phys. Rev. D **97**, 082002 (2018).
[95] K. Belczynski *et al.*, Astron. Astrophys. **636**, A104 (2020).
[96] D. Gerosa and E. Berti, Phys. Rev. D **95**, 124046 (2017).
[97] M. Fishbach, D. E. Holz, and B. Farr, Astrophys. J. Lett. **840**, L24 (2017).
[98] A. M. Hopkins and J. F. Beacom, Astrophys. J. **651**, 142 (2006).
[99] S. M. Wilkins, N. Trentham, and A. M. Hopkins, Mon. Not. R. Astron. Soc. **385**, 687 (2008).
[100] E. Vangioni, K. A. Olive, T. Prestegard, J. Silk, P. Petitjean, and V. Mandic, Mon. Not. R. Astron. Soc. **447**, 2575 (2015).
[101] M. D. Kistler, H. Yuksel, and A. M. Hopkins, arXiv:1305.1630.
[102] P. S. Behroozi and J. Silk, Astrophys. J. **799**, 32 (2015).
[103] R. J. Bouwens, G. D. Illingworth, P. A. Oesch, M. Trenti, I. Labbé, L. Bradley, M. Carollo, P. G. van Dokkum, V. Gonzalez, B. Holwerda, M. Franx, L. Spitler, R. Smit, and D. Magee, Astrophys. J. **803**, 34 (2015).
[104] E. Thrane and J. D. Romano, Phys. Rev. D **88**, 124032 (2013).
[105] LIGO-G1800243, https://dcc.ligo.org/LIGO-G1800243/public.
[106] B. Allen and J. D. Romano, Phys. Rev. D **59**, 102001 (1999).
[107] J. D. Romano and N. J. Cornish, Living Rev. Relativity **20**, 2 (2017).
[108] T. Callister, A. S. Biscoveanu, N. Christensen, M. Isi, A. Matas, O. Minazzoli, T. Regimbau, M. Sakellariadou, J. Tasson, and E. Thrane, Phys. Rev. X **7**, 041058 (2017).
[109] J. Aasi *et al.* (LIGO Scientific and Virgo Collaborations), Phys. Rev. D **91**, 022003 (2015).
[110] E. E. Flanagan, Phys. Rev. D **48**, 2389 (1993).
[111] V. Mandic, E. Thrane, S. Giampanis, and T. Regimbau, Phys. Rev. Lett. **109**, 171102 (2012).
[112] J. Buchner, A. Georgakakis, K. Nandra, L. Hsu, C. Rangel, M. Brightman, A. Merloni, M. Salvato, J. Donley, and D. Kocevski, Astro. Astrophys. **564**, A125 (2014).
[113] F. Feroz and M. P. Hobson, Mon. Not. R. Astron. Soc. **384**, 449 (2008).
[114] F. Feroz, M. P. Hobson, and M. Bridges, Mon. Not. R. Astron. Soc. **398**, 1601 (2009).
[115] F. Feroz, M. Hobson, E. Cameron, and A. Pettitt, Open J. Astrophys. **2**, 10 (2019).
[116] M. J. Stott, arXiv:2009.07206.
[117] H. Jeffreys, *Theory of Probability*, 3rd ed. (Oxford University Press, Oxford, England, 1961).
[118] T. Callister, L. Sammut, S. Qiu, I. Mandel, and E. Thrane, Phys. Rev. X **6**, 031018 (2016).
[119] A. Saffer and K. Yagi, Phys. Rev. D **102**, 024001 (2020).
[120] LIGO-T1900058, https://dcc.ligo.org/LIGO-T1900058/public.
[121] H. Krawczynski, Gen. Relativ. Gravit. **50**, 100 (2018).
[122] H. Yoshino and H. Kodama, Prog. Theor. Phys. **128**, 153 (2012).
[123] H. Yoshino and H. Kodama, Classical Quantum Gravity **32**, 214001 (2015).
[124] J. a. G. Rosa and T. W. Kephart, Phys. Rev. Lett. **120**, 231102 (2018).
[125] M. Boskovic, R. Brito, V. Cardoso, T. Ikeda, and H. Witek, Phys. Rev. D **99**, 035006 (2019).
[126] T. Ikeda, R. Brito, and V. Cardoso, Phys. Rev. Lett. **122**, 081101 (2019).
[127] H. Fukuda and K. Nakayama, J. High Energy Phys. 01 (2020) 128.
[128] A. Mathur, S. Rajendran, and E. H. Tanin, Phys. Rev. D **102**, 055015 (2020).
[129] A. Pierce, K. Riles, and Y. Zhao, Phys. Rev. Lett. **121**, 061102 (2018).
[130] H.-K. Guo, K. Riles, F.-W. Yang, and Y. Zhao, Commun. Phys. **2**, 155 (2019).
[131] A. L. Miller *et al.*, arXiv:2010.01925.
[132] Y. Michimura, T. Fujita, S. Morisaki, H. Nakatsuka, and I. Obata, Phys. Rev. D **102**, 102001 (2020).